# On the settling depth of meltwater escaping from beneath Antarctic ice shelves

Constantin W. Arnscheidt* and John Marshall

*Department of Earth, Atmospheric, and Planetary Sciences, Massachusetts Institute of Technology, Cambridge, MA, USA*

Pierre Dutrieux

*British Antarctic Survey, Natural Environment Research Council, Cambridge, UK and Lamont-Doherty Earth Observatory of Columbia University, Palisades, NY, USA*

Craig D. Rye

*Department of Earth, Atmospheric, and Planetary Sciences, Massachusetts Institute of Technology, Cambridge, MA, USA and Goddard Institute for Space Studies, New York City, NY, USA*

Ali Ramadhan

*Department of Earth, Atmospheric, and Planetary Sciences, Massachusetts Institute of Technology, Cambridge, MA, USA*

**Corresponding author*: Constantin W. Arnscheidt, cwa@mit.edu

ABSTRACT

Antarctic glacial meltwater likely plays an important role in determining large-scale Southern Ocean climate trends, yet recent modeling efforts have proceeded without a good understanding of how its vertical distribution in the water column is set. To rectify this, here we conduct new large-eddy simulations of a buoyant meltwater plume escaping from underneath an Antarctic ice shelf. We find that the meltwater's settling depth is primarily a function of the buoyancy forcing per unit width and the ambient stratification, consistent with the classical theory of turbulent buoyant plumes and in contrast to previous work that suggested an important role for centrifugal instability. Our results further highlight the significant role played by the variability in stratification; this helps explain observed interannual variability in the vertical meltwater distribution near Pine Island Glacier. Because of the vast heterogeneity in mass loss rates from different Antarctic ice shelves, a dynamic parameterization of meltwater settling depth may be crucial for accurately simulating high-latitude climate in a warming world; the work presented in this study is a first step towards its development.

## 1. Introduction

A notable failure of the global coupled climate models included in the Coupled Model Intercomparison Project Phase 5 (CMIP5, Taylor et al. 2012) has been their inability to hindcast important observed Southern Ocean climate trends such as surface cooling, surface freshening, and sea-ice expansion (Turner et al. 2013; Jones et al. 2016; Kostov et al. 2018). Recent work suggests that the increase in Antarctic meltwater anomaly over this period may have played an important role in driving the observed trends. Climate models typically neglect the freshwater flux due to net mass loss from the Antarctic ice sheet: this has increased over the past few decades to around 500 Gt/yr (Paolo et al. 2015; Rignot et al. 2019). Recent work suggests that the incorporation of this process into climate models could help to explain the observed trends, resolving the discrepancy (Bintanja et al. 2013; Rye et al. 2014; Bintanja et al. 2015; Rye et al. 2020). The incorporation of Antarctic glacial meltwater also has a significant impact on projections of future climate. (Bronselaer et al. 2018; Golledge et al. 2019). Although there remains some disagreement about the magnitude of the climate impacts due to meltwater (Swart and Fyfe 2013; Pauling et al. 2016), understanding how to correctly represent this process in global climate models is clearly of importance.

In climate modeling studies, the meltwater has generally been represented as an externally imposed freshwater flux; this requires a starting assumption about where in the water column the glacial meltwater is situated. In many studies, glacial meltwater has been introduced at or near the surface (Bintanja et al. 2013; Swart and Fyfe 2013; Rye et al. 2014; Bintanja et al. 2015; Hansen et al. 2016; Pauling et al. 2016; Bronselaer et al. 2018), or over a constant depth (Rye et al. 2020). Even though most of the melting occurs at depth, the meltwater might be expected to rise to the surface due to its relatively low density; however, this assumption is not supported by observations. For example, measurements of noble gas concentrations in the Ross Sea (Loose et al. 2009) and in the Amundsen Sea (Kim et al. 2016; Biddle et al. 2019) reveal vertical meltwater distributions centered at around 300m-400m depth. Near Pine Island Glacier, which is the source of a large fraction of the total Antarctic melt, Dutrieux et al. (2014) found large interannual variability in meltwater settling depth, with meltwater settling close to the surface in some years and hundreds of meters at depth in other years. A better understanding of what determines the settling depth of Antarctic glacial meltwater may greatly improve our understanding of ice-ocean interactions as well as their representation in climate models.

Aspects of glacial meltwater dynamics have been studied previously. In the Antarctic context, the priority has been to determine the rate and spatial distribution of sub-ice-shelf melting for given boundary conditions and forcings. To this end, studies have employed one-dimensional plume models (MacAyeal 1985; Jenkins 1991, 2011; Lazeroms et al. 2018), box models (Olbers and Hellmer 2010; Reese et al. 2018), and three-dimensional fluid dynamics simulations on the ice-shelf scale (Losch 2008; De Rydt et al. 2014; Mathiot et al. 2017). In an Arctic context, where glaciers generally exhibit a near-vertical ice face for the entire depth of the water column instead of an ice shelf cavity, meltwater dynamics have been studied using high-resolution numerical simulations of individual (Xu et al. 2012, 2013; Sciascia et al. 2013) and distributed (Carroll et al. 2015; Slater et al. 2015) plumes. Again, it was largely the spatial distribution of melting that was emphasized, together with implications for the fjord-scale circulation. Finally, Naveira Garabato et al. (2017) have studied the small-scale fluid dynamics of meltwater escaping from underneath an Antarctic ice shelf, with an explicit focus on meltwater settling depth. They employed a two-dimensional simulation of the meltwater outflow to argue that centrifugal instability, which contributes to lateral mixing of the rising meltwater plume, plays a dominant role in controlling the settling depth.

In this study, we revisit the small-scale fluid dynamics of meltwater escape from underneath an ice shelf. First, we describe an idealized glacial meltwater outflow, and introduce simple models for the meltwater's settling depth. Second, we describe new three-dimensional large-eddy simulations of the meltwater outflow, and compare the results to the predictions of the simpler models. Third, we use our models to address observed interannual variability in meltwater settling depth near Pine Island Glacier. Finally, we discuss why a dynamic parameterization of meltwater settling depth could be crucial for accurately simulating high-latitude climate, and outline how such a parameterization could be implemented building on the work in this study.

## 2. Theory and Methods

The object of this study is described schematically in Figure 1. Much of the total mass loss from the Antarctic ice sheet stems from a small number of rapidly-melting ice shelves; here, we focus on Pine Island Glacier, which is the source of a large fraction of the total mass loss. The meltwater outflow from underneath the Pine Island ice shelf is concentrated in a narrow km-scale flow at its western edge (Thurnherr et al. 2014; Naveira Garabato et al. 2017). This narrow meltwater outflow is likely a generic feature of many Antarctic ice shelves, as it is a straightforward consequence of a typical sub-ice-shelf circulation (e.g. Grosfeld et al. 1997; Losch 2008). We investigate the dynamics of such a meltwater outflow by idealizing it as a fixed buoyancy source $F$, with width $L$, applied to the bottom of our model domain. In this section, we outline the hierarchy of theoretical and modeling approaches that we will use.

### *a. Simple scaling relationships*

The glacial meltwater escaping from underneath the ice shelf undergoes turbulent buoyant convection in a stratified ambient fluid. The theory of such processes was first developed by

Morton et al. (1956). For plumes originating from a point source, far from any walls, this theory has yielded robust scaling laws for the plume's rise height in terms of the buoyancy source $F$ and the background buoyancy frequency $N$. These scaling laws have been repeatedly confirmed in laboratory and experimental work (Turner 1986; Helfrich and Battisti 1991; Speer and Marshall 1995; Fabregat Tomàs et al. 2016). As described, for example, by Speer and Marshall (1995), as long as $N$ is substantially larger than the Coriolis parameter $f$, the only two parameters that could physically control the rise height are $F$ ($m^4/s^3$, consider an area-integrated buoyancy flux) and $N$ ($s^{-1}$). Dimensional analysis then yields a vertical scale

$$h_N = \left(\frac{F}{N^3}\right)^{\frac{1}{4}}. \tag{1}$$

The real rise height $h$ is proportional to this vertical scale:

$$h = a h_N, \tag{2}$$

where $a$ is a constant. Numerical experiments consistently yield a value of $a \simeq 2.6$ (e.g. Speer and Marshall 1995; Fabregat Tomàs et al. 2016).

In the case of the glacial meltwater outflow, however, the meltwater plume does not originate from a point source: it is rather in the shape of a line, where the total buoyancy forcing $F$ is distributed over some width $L$ (see Figure 1). Therefore, we modify equation (1) by assuming that the two parameters exerting control over the rise height are the buoyancy source per unit width, $F/L$ ($m^3/s^3$), and the background buoyancy frequency, $N$ ($s^{-1}$). Dimensional analysis now yields a vertical scale of

$$h_N = \left(\frac{F}{L}\right)^{\frac{1}{3}} \frac{1}{N}. \tag{3}$$

Again, the real rise height is proportional to this scale:

$$h = a h_N, \tag{4}$$

where the constant of proportionality could be expected to match the value observed for plumes originating from a point source ($a \simeq 2.6$).

### b. *One-dimensional line plume model*

The scaling theory described above cannot account for the effects of non-uniform stratification (i.e. $N = N(z)$), and provides only limited physical insight. To improve upon it, we can follow Morton et al. (1956) in constructing a one-dimensional vertical steady-state model of the buoyant plume. The original model of Morton et al. (1956) describes a point buoyancy source, and has been previously adapted to consider a point source of meltwater next to a vertical wall (Carroll et al. 2015). One-dimensional models of buoyant line plumes rising underneath a sloping interface have also been widely applied to the study of sub-ice-shelf meltwater dynamics (MacAyeal 1985; Jenkins 1991, 2011; Lazeroms et al. 2018; Pelle et al. 2019). These models generally consider explicit fluxes of heat and salt instead of a generic buoyancy flux, as well as interactions across the ice-ocean interface.

Throughout this study we will assume that the dominant contribution to meltwater production is made below the ice shelf and that thermodynamic interactions between the plume and the ice shelf front itself (see Figure 1) are negligible. For a buoyant plume originating from a line source next to a vertical wall, these assumptions lead to the following system of coupled ordinary differential equations (see Appendix A):

$$\frac{dQ}{dz} = \alpha \frac{M}{Q} \tag{5}$$

$$\frac{dM}{dz} = \frac{QB}{M} \tag{6}$$

$$\frac{dB}{dz} = -QN^2. \tag{7}$$

Here $Q$, $M$, and $B$ are vertical fluxes per unit length of volume, momentum, and buoyancy, respectively. $N(z)$ is the buoyancy frequency, $g$ is the acceleration due to gravity, and $\alpha$ is a non-dimensional entrainment coefficient. The model is solved for a given buoyancy forcing $F/L$ by setting $B = F/L$ at the bottom of the domain and integrating upwards. The meltwater's settling depth is then given by the level of neutral buoyancy, which is where $B(z) = 0$. Since $F/L$ and $N$ are the only dimensional input parameters, a characteristic vertical scale is again given by $h_N = (F/L)^{1/3}/N$.

Example solutions of this one-dimensional model are shown in Figure 2, for a range of buoyancy forcings $F/L$. Here, the background buoyancy frequency $N = 3 \times 10^{-3}$ s$^{-1}$, a realistic value for Pine Island Bay. Values used for the entrainment coefficient vary across the literature; here, we use $\alpha = 0.15$, which is consistent with effective entrainment coefficients calculated from past numerical simulations of hydrothermal plumes (Jiang and Breier 2014; Fabregat Tomàs et al. 2016). We integrate our model equations using an eighth-order Runge-Kutta method (Prince and Dormand 1981).

### *c. Three-dimensional large-eddy simulations*

To accurately study the behavior of the buoyant plume, and to evaluate the utility of the simpler theories described above, we need to conduct high-resolution simulations of the underlying small-scale fluid dynamics. Many previous studies have simulated the dynamics of hydrothermal plumes rising far from any walls (e.g. Lavelle 1995; Speer and Marshall 1995; Jiang and Breier 2014; Fabregat Tomàs et al. 2016). In the Arctic context, two-dimensional and three-dimensional simulations of glacial meltwater plumes have been conducted (Xu et al. 2012, 2013; Sciascia et al. 2013; Carroll et al. 2015); these studies emphasized the spatial distribution of melting and the fjord-scale circulation. Meltwater escape from underneath an Antarctic ice shelf has been previously simulated in two dimensions by Naveira Garabato et al. (2017), who also based their simulations on an idealization of the outflow from below the Pine Island ice shelf.

All of these numerical simulations of glacial meltwater plumes have used the Massachusetts Institute of Technology general circulation model in a non-hydrostatic configuration (MITgcm, Marshall et al. 1997). Here, we conduct new three-dimensional large-eddy simulations of a line glacial meltwater plume rising next to a wall using the software package Oceananigans.jl (Ramadhan et al. 2020). Oceananigans.jl is written in the high-level Julia programming language (Bezanson et al. 2017), simulates the rotating non-hydrostatic incompressible Boussinesq equations using a finite volume discretization similar to that of the MITgcm, and is optimized to run on Graphical Processing Units (GPUs). The equations are integrated using a second-order Adams-Bashforth scheme with adaptive time stepping. The effects of sub-grid scale processes are parameterized via an eddy viscosity and eddy diffusivity modeled using the anisotropic minimum dissipation (AMD) large-eddy simulation closure (Rozema et al. 2015). The AMD formalism was refined by Verstappen (2018) and validated for ocean-relevant scenarios by Vreugdenhil and Taylor (2018).

Our model domain follows the schematic in Figure 1. The horizontal widths $L_y$ and $L_x$ are both set to 5 km, while the depth of the ice shelf front $L_z$ is set equal to 400m (approximately consistent with Pine Island Glacier, see Jenkins et al. 2010). The domain is re-entrant in the zonal $x$-direction. We use 512 grid cells in each horizontal direction and 96 grid cells in the vertical: this corresponds to a horizontal resolution of 9.77 m and a vertical resolution of 4.17 m. We consider the evolution of temperature, salinity, and a passive tracer representing meltwater. Glacial meltwater escaping from underneath the ice shelf is represented as a constant buoyancy source $F$ applied to a horizontal area of length $L$ next to the southern edge of the domain (see Figure 1). $L$ is set to 1 km; as previously discussed, the meltwater from beneath Pine Island glacier is concentrated in a narrow outflow broadly consistent with this scale (Naveira Garabato et al. 2017). The buoyancy source $F$ is implemented as a constant volume-conserving “virtual salinity flux"

(Huang 1993; see Appendix B for details). The Coriolis parameter, $f$, is set to $-1.4\times10^{-4}$ s$^{-1}$, appropriate for the latitude of Pine Island.

## 3. Results

### *a. The simulated meltwater plume*

The basic behavior of the simulated glacial meltwater plume is demonstrated in Figure 3; here, $F/L = 10^{-2}$ m$^3$/s$^3$. As in Figure 2, the initial condition is a uniform buoyancy frequency of $N = 3\times10^{-3}$ s$^{-1}$; this yields $N/f \simeq 20$, similar to the meltwater plume simulations of Naveira Garabato et al. (2017). For now, the stratification is implemented through a linear vertical salinity gradient, fixed temperature, and a linear equation of state with haline contraction coefficient $\beta = 7.8\times10^{-4}$ psu$^{-1}$ (Vallis 2017). Following the evolution of the passive meltwater tracer, we see that the turbulent plume initially rises rapidly, and then moves northward once it reaches neutral buoyancy. The northward flow is deflected to the left by the Coriolis force, resulting in a strong westward jet; this is consistent with the observations and two-dimensional simulations of Naveira Garabato et al. (2017).

Next, we consider the time evolution of the horizontally averaged meltwater distribution over one day of simulation. To quantify the effect that the Earth's rotation may play in determining the plume's settling depth (e.g. Fabregat Tomàs et al. 2016; Naveira Garabato et al. 2017), we conduct two simulations: one where the Coriolis parameter $f$ has a realistic value $-1.4\times10^{-4}$ s$^{-1}$, and one where $f$ has been set to zero. The results of these experiments are shown in Figure 4. We observe that, for this realistic choice of $N/f$, the meltwater's settling depth is essentially determined on a timescale $N^{-1}$: the non-rotating and rotating experiments both yield similar mean settling depths. However, the rotating experiment shows a distinct broadening of the vertical meltwater distribution as we approach a timescale of 1 day, suggestive of rotational effects playing an important mixing role.

Interestingly, these results conflict with those of Naveira Garabato et al. (2017), who used two-dimensional simulations to argue that centrifugal instability is a dominant mechanism controlling the settling depth of the meltwater. As the northward-moving meltwater is deflected to the left by the Coriolis force, a strong zonal jet develops (Figure 3); centrifugal instability can occur if the resulting anticyclonic vorticity is large enough ($\zeta/f < -1$, Haine and Marshall 1998), promoting lateral export and mixing of the meltwater. In their two-dimensional simulations, Naveira Garabato et al. (2017), observed over the same timeframe of 1 day that setting $f = -1.4 \times 10^{-4}$ s$^{-1}$ was sufficient to deepen the peak of the meltwater distribution by $\sim$ 50 m compared to the case with $f$ = 0, a substantial effect that is not present in Figure 4. In Appendix C we address this discrepancy using additional two-dimensional simulations: those results suggest that the effect observed in the simulations of Naveira Garabato et al. (2017) may be related to their use of a restoring buoyancy source formulation rather than a constant buoyancy source formulation as implemented in this study. Here, we simply conclude that, for realistic values of $N/f$, rotational effects seem to play a negligible role in determining the meltwater's settling depth.

### *b. Vertical meltwater distribution: uniform stratification*

Now, we can evaluate how the meltwater's settling depth depends on the buoyancy source and the background stratification. We conduct a set of simulations where $F/L$ and $N$ are separately varied: the vertical meltwater distributions after 6 hours of integration are shown in Figure 5. We choose this timescale because by this point the settling depth has been essentially determined (Figure 4). The default values of $F/L$ and $N$ in Figure 5 are $10^{-2}$ m$^3$/s$^3$ and $3 \times 10^{-3}$ s$^{-1}$. For the case of varying $F/L$ we included as an additional x-axis an estimate of the corresponding glacial mass loss due to melt, divided by the outflow width; details are described in Appendix D. On top of the distributions obtained from the simulations we also plot predictions from the simple scaling solution (eq. 3, $a = 2.6$) and the one-dimensional line plume model presented above. Both show excellent agreement with the high-resolution simulations, suggesting that they parametrize the settling depth extremely well in these idealized conditions.

### *c. Vertical meltwater distribution: non-uniform stratification*

In the real world, the buoyancy frequency $N$ is non-uniform in time and space. For example, observations from Pine Island Bay show that vertical profiles of temperature, salinity, and meltwater fraction show significant interannual variability (Dutrieux et al. 2014). In Figure 6 we demonstrate this variability by plotting temperature and salinity profiles collected next to the meltwater outflow from Pine Island Glacier in 2009 and 2014 (Jacobs et al. 2011; Heywood et al. 2016), together with estimates of the corresponding meltwater fractions. Notably, in 2009 meltwater was primarily centered at a depth of 400m, while in 2014 it was able to rise to the surface. This difference appears too dramatic to be explained purely by interannual variability in melt rates (consider the $h \propto F^{1/3}$ scaling); hence, we propose that the variability in stratification played a major role.

We investigate the effect of the different background conditions in 2009 and 2014 by using the top 400m of the observed temperature and salinity profiles as our initial conditions in our high-resolution simulations. From these, Oceananigans.jl calculates a density profile using the idealized nonlinear equation of state proposed by Roquet et al. (2015), optimized for near freezing. We consider two different buoyancy sources, $F/L = 10^{-3}$ m$^3$/s$^3$ and $F/L = 10^{-2}$ m$^3$/s$^3$. The vertical meltwater distributions after 6 hours are shown in Figure 7. We additionally plot an estimate of the strength of the stratification as a function of depth; this is obtained by calculating $N^2 = -\frac{g}{\rho_0}\frac{d\rho}{dz}$ on a point-wise basis and applying a moving average with a 20m window to isolate larger-scale trends.

For the case of $F/L = 10^{-2}$ m$^3$/s$^3$, we see that there is little difference in the vertical meltwater distribution between 2009 and 2014 conditions. However, the simulations with $F/L = 10^{-3}$ m$^3$/s$^3$ show a marked difference: in the 2009 case, meltwater settles at ~350 m depth, while in the 2014 case it rises around 100m shallower. The qualitative trend is consistent with the observations (Figure 6). Finally, we have also plotted the settling depths predicted by the one-dimensional plume model: there is near-perfect agreement with the peaks of the meltwater distributions obtained from our high-resolution simulations.

We suggest that this difference in behaviors for the $F/L = 10^{-3}$ m$^3$/s$^3$ case can be simply explained by changes in the background stratification. Namely, in 2009 there was a marked peak in $N^2$ at around 350m depth that was not present in 2014. The meltwater settling at this very depth in the simulations is thus an indication that it was "trapped" by the local maximum in stratification. When the buoyancy source was larger ($F/L = 10^{-2}$ m$^3$/s$^3$), the meltwater was able to "break through" the stratification maximum, and ended up with a vertical distribution very similar to the corresponding 2014 stratification profile.

## 4. Discussion

The potency of Antarctic glacial meltwater as a driver of regional and global climate trends likely depends strongly on its settling depth or vertical distribution after exiting the ice shelf cavity. Specifically, it seems feasible that meltwater could only explain the signs of the observed Southern ocean trends (surface cooling, surface freshening, and sea-ice expansion) as long as it rises close enough to the surface to shoal the mixed layer and to yield a measurable surface salinity anomaly. Pauling et al. (2016), who considered the effects of releasing freshwater at different depths, found that the depth of meltwater release had no significant effect on the magnitude of sea-ice expansion; however, they also found a much weaker response of sea-ice expansion to freshwater forcing than other studies (Bintanja et al. 2013, 2015; Rye et al. 2020). The causes of these inter-model differences are poorly understood. This issue was highlighted by the recent work of Naveira Garabato et al. (2017), which uses observations and an idealized model to suggest that centrifugal instability acts to rapidly distribute melt water laterally, reducing its potency to the surface climate; however, other observations (e.g. Dutrieux et al. 2014) suggest that meltwater can settle at a range of depths in the Subpolar Sea, implying that time-varying environmental conditions and the properties of the meltwater plume play important roles in determining the vertical distribution of settled meltwater in the Shelf Seas and therefore the climate impact of meltwater anomaly production. The role that the depth of meltwater release plays remains very far from settled, and deserves further study.

In Figure 8, we identify two different paradigms for introducing glacial meltwater fluxes into high-latitude oceans for simulations of global climate. In paradigm A, the fluxes calculated by a melt rate model are inserted into the ocean model at some fixed vertical level. This paradigm has dominated the literature: as described earlier, most climate modeling studies have introduced all of the meltwater flux at the surface. In other studies, the meltwater has been uniformly distributed over a fixed range of depths below the ice shelf front (Beckmann and Goosse 2003; Mathiot et al. 2017). Given the likely climatic importance of glacial meltwater, the strong dependence of settling depth on buoyancy release (e.g. as explored in this study), and the vast heterogeneity in the observed mass loss rates from different ice shelves (Rignot et al. 2019), any such "one-size-fits-all" solution risks missing substantial aspects of the climate response to Antarctic mass loss. However, an alternative approach is possible: in paradigm B, the melt rate model is coupled to a dynamic plume model that describes the small-scale dynamics of buoyant meltwater plumes and accurately calculates the vertical distribution of meltwater. The meltwater is then inserted into the ocean model in accordance with this distribution.

The work done in this study serves as a first step towards developing such a dynamic meltwater plume parameterization, although some issues still remain to be solved. As indicated in Figure 7, the simple one-dimensional plume model accurately predicts the peak of the vertical meltwater distribution even for complex non-uniform stratification. The fact that many sub-ice-shelf melt-rate parameterizations are based on similar models of a sloping plume (Jenkins 2011; Lazeroms et al. 2018; Pelle et al. 2019) suggests that a single appropriately specified model could potentially calculate both the melt rates and the meltwater settling depth. One challenge with this kind of formulation would be dealing with the large discontinuous jump in slope that occurs at the bottom of the ice shelf front; here, we have considered only the part of the plume next to the front, idealizing the meltwater outflow from below as a constant buoyancy source. Another issue relates to a fundamental limitation of the one-dimensional view; it neglects the along-shelf dynamics, which have been shown to significantly affect total melt rates in the Arctic context (Jackson et al. 2020). The most significant limitation with respect to computing meltwater settling depths, however, is that these one-dimensional parameterizations can only output a single meltwater settling depth ($B(z) = 0$). Meanwhile, observed vertical meltwater distributions can have complex, possibly multi-modal shapes. Short of explicitly resolving the small-scale fluid dynamics of the meltwater plume next to and below the entire ice shelf, it may be possible to extend upon the one-dimensional plume model, perhaps by introducing a time dependence, to explicitly include a passive meltwater tracer that would allow for the calculation of a vertical distribution rather than just its peak.

## 5. Conclusion

Antarctic glacial meltwater is likely an important driver of observed Southern Ocean climate trends (Bintanja et al. 2013; Rye et al. 2014; Bintanja et al. 2015; Rye et al. 2020), and will have a significant impact throughout the twenty-first century (Bronselaer et al. 2018; Golledge et al.

2019). Nevertheless, the factors determining the vertical distribution of meltwater in the water column remain poorly understood. Here, we have used a hierarchy of approaches, spanning simple scaling laws to high-resolution large-eddy simulations of the meltwater outflow from beneath an ice shelf, to gain a fundamental understanding of the most important controls on the meltwater's settling depth. We found that the settling depth is primarily a function of the buoyancy forcing per unit width and the ambient stratification, consistent with the classical theory of turbulent buoyant plumes and in constrast to previous suggestions that centrifugal instability plays an important role (Naveira Garabato et al. 2017). Our simulations also provide insight into the observed interannual variability in meltwater settling depth, using Pine Island Glacier as an example; the role of the non-uniform background stratification is highlighted. Because the focusing of sub-ice-shelf meltwater into a narrow outflow is a basic consequence of a generic sub-ice-shelf circulation (Grosfeld et al. 1997; Losch 2008; De Rydt et al. 2014), we expect that the results of this study are relevant to a wide range of Antarctic ice shelves. The work presented in this study is the first step towards a dynamic parameterization of meltwater settling depth for simulations of global climate. Because of the likely climatic importance of glacial meltwater, the strong dependence of mass loss rates on buoyancy forcing, and the vast heterogeneity in observed mass loss rates from different ice shelves, such a parameterization could be crucial for the accurate simulation and forecasting of high-latitude climate in a warming world.

*Acknowledgments.* We thank Alberto Naveira Garabato for discussions that helped motivate this work, and Gianluca Meneghello and Jean-Michel Campin for discussions that aided in its execution. J. M. and C. D. R. acknowledge support from the NASA MAP program and the MIT-GISS cooperative agreement. A. R. was supported through the CliMA initiative funded by the Eric and Wendy Schmidt foundation. P. D. was supported by NSF OPP award 1643285 and his Center for Climate and Life Fellowship from the Earth Institute of Columbia University.

*Data availability statement.* This study generated no new data. Code for the one-dimensional line plume model and the two- and three-dimensional large-eddy simulations is available at https://github.com/arnscheidt/antarctic-meltwater-settling-depth.

## APPENDIX A

## One-dimensional line plume model

We construct a 1-dimensional vertical line plume model in the spirit of Morton et al. (1956). Here, the rate of turbulent entrainment of ambient fluid into the rising buoyant plume is parametrized as proportional to the plume's vertical velocity via an entrainment coefficient, $\alpha$. We assume that the vertical velocity $w$ is uniform within the plume and zero outside, and that the plume is rising next to a wall (so that entrainment can only occur from one side). We can then write down volume, momentum, and mass conservation equations within the plume:

$$\frac{d}{dz}(Dw) = \alpha w \tag{A1}$$

$$\frac{d}{dz}(Dw\rho w) = Dg(\rho_a - \rho) \tag{A2}$$

$$\frac{d}{dz}(Dw\rho) = \alpha w \rho_a. \tag{A3}$$

Here, $\rho(z)$ is the density of the plume, $\rho_a(z)$ is the ambient density, $D$ is the width of the plume perpendicular to the wall, and $\alpha$ is the entrainment coefficient. Assuming that $\rho(z)$ differs only slightly from the reference density $\rho_0$, we can rewrite Equation (A2) as

$$\frac{d}{dz}(Dw^2) = D\frac{g}{\rho_0}(\rho_a - \rho). \tag{A4}$$

Following the reasoning in Morton et al. (1956), we can use Equation (A1) to rewrite Equation (A3) as

$$\frac{d}{dz}(Dw\rho) = \rho_a \frac{d}{dz}(Dw) = \frac{d}{dz}(Dw\rho_a) - Dw\frac{d}{dz}\rho_a, \tag{A5}$$

such that

$$\frac{d}{dz}(Dw(\rho_a - \rho)) = Dw\frac{d\rho_a}{dz}. \tag{A6}$$

Now, writing $Dw = Q$ (volume flux), $Dw^2 = M$ (momentum flux) and $Dwg\frac{(\rho_a-\rho)}{\rho_0} = B$ (buoyancy flux), we obtain the three coupled ODEs

$$\frac{dQ}{dz} = \alpha\frac{M}{Q} \tag{A7}$$

$$\frac{dM}{dz} = \frac{QB}{M} \tag{A8}$$

$$\frac{dB}{dz} = Q\frac{g}{\rho_0}\frac{d\rho_a}{dz} = -QN^2. \tag{A9}$$

These equations are similar but not equivalent to the corresponding equations for point plumes. Furthermore, each of the three governing equations has implicitly been divided by a factor of $L$ (x-width of the plume); thus, all of the quantities $Q, M, B$ are fluxes per unit width.

## APPENDIX B

## Buoyancy source implementation

We implement the buoyancy source $F$ ($m^4/s^3$) in our high-resolution simulations as a volume-conserving "virtual salinity flux" (Huang 1993). The conservation law for an arbitrary tracer $c$ in Oceananigans.jl is

$$\frac{\partial c}{\partial t} + \mathbf{u}\cdot\nabla c = -\nabla\cdot\mathbf{q_c} + F_c, \tag{B1}$$

where $\mathbf{q_c}$ is a diffusive flux and $F_c$ is an external source term. In our simulations, we introduce the buoyancy uniformly across a volume that extends width $L$ in the $x$-direction, 10 grid cells in the

$y$-direction ($\sim$ 100 m), and one grid cell in the $z$-direction ($\sim$ 4 m), Defining this volume as $V_B$, we can write

$$\int_{V_B} dV \frac{db}{dt}_{\text{source}} = F, \tag{B2}$$

where $\frac{db}{dt}_{\text{source}}$ refers only to the term within the full buoyancy conservation equation that comes from the external buoyancy source. Now, recall that

$$b = -\frac{g}{\rho_0}(\rho - \rho_0), \tag{B3}$$

and that, to first order,

$$\rho = \rho_0(1 - \alpha(T - T_0) + \beta(S - S_0)). \tag{B4}$$

Thus, if no temperature forcing is introduced,

$$\frac{db}{dt}_{\text{source}} = \frac{db}{d\rho}\frac{d\rho}{dt}_{\text{source}} = -\frac{g}{\rho_0}\frac{d\rho}{dt}_{\text{source}} = -g\beta\frac{dS}{dt}_{\text{source}}, \tag{B5}$$

and, by (B2):

$$F = -\int_{V_B} dV g\beta \frac{dS}{dt}_{\text{source}} \equiv -g\beta F_S, \tag{B6}$$

where $F_S$ is the volume-integrated salinity flux (psu m$^3$/s). For a chosen $F$ we therefore obtain a corresponding $F_S$ by (B6). Then, in our simulations, we distribute $F_S$ uniformly across $V_B$.

## APPENDIX C

### Restoring buoyancy sources may exaggerate the importance of rotational effects in determining the meltwater's settling depth

Our results conflict with those of Naveira Garabato et al. (2017). Using a two-dimensional model, they found that including realistic rotation deepened the peak of the observed meltwater distribution by $\sim$ 50 m compared to a non-rotating case, after one day of integration. To clarify why there is a discrepancy, we conduct additional two-dimensional simulations with Oceananigans.jl that are designed to closely replicate those of Naveira Garabato et al. (2017).

The model domain spans 5km × 300m and is zonally re-entrant. Our resolution is $512 \times 96$, i.e. ~10m×3m. The initial stable stratification is implemented using a linear equation of state and a linear temperature gradient from 1 °C at the bottom to 3 °C at the top. At the northern boundary, we continuously relax back to the stable initial condition. At the base of the southern boundary we introduce meltwater via an unstable restoring region that extends 160m in the y-direction. In the unstable restoring region, temperature is relaxed to a temperature $T_r(y)$, which is set following a linear gradient: its value is 2 °C at $y = 0$ m and 1 °C at $y = 160$ m. For clarity, in the buoyancy source region:

$$\frac{dT}{dt} = (\text{other terms}) + \lambda(T_r(y) - T), \tag{C1}$$

where $\lambda = 1/20$ s$^{-1}$. This experiment is conducted twice, once with $f = -1.4 \times 10^{-4}$ s$^{-1}$ (realistic rotation) and once with $f = 0$ (no rotation). We then conduct an additional set of simulations using a constant buoyancy source, which is set to approximately yield the same settling depth.

Figure 9 shows the vertical distribution of glacial melt in the water column after 1 day, for both rotating and non-rotating cases, and for a restoring formulation and a constant buoyancy source formulation. When a restoring formulation is used, in the rotating case the peak is ~ 50 m deeper than in the non-rotating case, consistent with the results of Naveira Garabato et al. (2017). However, when a constant buoyancy source is used, rotation appears to have no effect on the peak of the meltwater distribution. Since the magnitude of the buoyancy source is a primary control on the meltwater's settling depth, the importance of any other parameters can only be accurately investigated by holding the buoyancy source constant. This suggests that the bottom results in Figure 9 are more physical, and that the use of restoring non-constant buoyancy sources may exaggerate the effect of rotation on the settling depth.

# APPENDIX D

## Estimating the glacial mass loss due to melt that corresponds to a given buoyancy source

For the second $x$-axis included in Figure 5, we have estimated the glacial mass loss due to melt that corresponds to a given buoyancy source $F$ ($m^4/s^3$). For this conversion, we have assumed that the input of a given volume of freshwater into the system is equivalent to the removal of that same volume of water at a reference salinity $S_0$ (set to 34.6). This can be justified rigorously by noting that, if we add a small volume of water $\Delta V$ with salinity 0 to a large volume of water $V$ with salinity $S$, the new salinity is given by

$$S + \Delta S = \frac{VS}{V + \Delta V} \simeq S(1 - \frac{\Delta V}{V}) \tag{D1}$$

i.e.

$$V\Delta S \simeq -S\Delta V. \tag{D2}$$

Defining an equivalent mass loss flux $F_M$ (kg/s), we have, following (B6),

$$F_M \simeq \rho_0 \frac{F_S}{S_0} = \frac{\rho F}{g\beta S_0}. \tag{D3}$$

The quantity measured by the second $x$-axis in Figure 5 is $F_M$ divided by the outflow width $L$.

## References


Beckmann, A., and H. Goosse, 2003: A parameterization of ice shelf–ocean interaction for climate models. *Ocean modelling*, **5 (2)**, 157–170.

Bezanson, J., A. Edelman, S. Karpinski, and V. B. Shah, 2017: Julia: A fresh approach to numerical computing. *SIAM review*, **59 (1)**, 65–98.

Biddle, L. C., B. Loose, and K. J. Heywood, 2019: Upper ocean distribution of glacial meltwater in the amundsen sea, antarctica. *Journal of Geophysical Research: Oceans*, **124 (10)**, 6854–6870.

Bintanja, R., G. Van Oldenborgh, S. Drijfhout, B. Wouters, and C. Katsman, 2013: Important role for ocean warming and increased ice-shelf melt in antarctic sea-ice expansion. *Nature Geoscience*, **6 (5)**, 376.

Bintanja, R., G. Van Oldenborgh, and C. Katsman, 2015: The effect of increased fresh water from antarctic ice shelves on future trends in antarctic sea ice. *Annals of Glaciology*, **56 (69)**, 120–126.

Bronselaer, B., M. Winton, S. M. Griffies, W. J. Hurlin, K. B. Rodgers, O. V. Sergienko, R. J. Stouffer, and J. L. Russell, 2018: Change in future climate due to antarctic meltwater. *Nature*, **564 (7734)**, 53.

Carroll, D., D. A. Sutherland, E. L. Shroyer, J. D. Nash, G. A. Catania, and L. A. Stearns, 2015: Modeling turbulent subglacial meltwater plumes: Implications for fjord-scale buoyancy-driven circulation. *Journal of Physical Oceanography*, **45 (8)**, 2169–2185.

De Rydt, J., P. Holland, P. Dutrieux, and A. Jenkins, 2014: Geometric and oceanographic controls on melting beneath pine island glacier. *Journal of Geophysical Research: Oceans*, **119 (4)**, 2420–2438.

Dutrieux, P., and Coauthors, 2014: Strong sensitivity of pine island ice-shelf melting to climatic variability. *Science*, **343 (6167)**, 174–178.

Fabregat Tomàs, A., A. C. Poje, T. M. Özgökmen, and W. K. Dewar, 2016: Effects of rotation on turbulent buoyant plumes in stratified environments. *Journal of Geophysical Research: Oceans*, **121 (8)**, 5397–5417.

Golledge, N. R., E. D. Keller, N. Gomez, K. A. Naughten, J. Bernales, L. D. Trusel, and T. L. Edwards, 2019: Global environmental consequences of twenty-first-century ice-sheet melt. *Nature*, **566 (7742)**, 65–72.

Grosfeld, K., R. Gerdes, and J. Determann, 1997: Thermohaline circulation and interaction between ice shelf cavities and the adjacent open ocean. *Journal of Geophysical Research: Oceans*, **102 (C7)**, 15 595–15 610.

Haine, T. W., and J. Marshall, 1998: Gravitational, symmetric, and baroclinic instability of the ocean mixed layer. *Journal of physical oceanography*, **28 (4)**, 634–658.

Hansen, J., and Coauthors, 2016: Ice melt, sea level rise and superstorms: evidence from paleoclimate data, climate modeling, and modern observations that 2 c global warming is highly dangerous. *Atmospheric Chemistry & Physics Discussions*, **16 (6)**.

Helfrich, K. R., and T. M. Battisti, 1991: Experiments on baroclinic vortex shedding from hydrothermal plumes. *Journal of Geophysical Research: Oceans*, **96 (C7)**, 12 511–12 518.

Heywood, K. J., and Coauthors, 2016: Between the devil and the deep blue sea: the role of the amundsen sea continental shelf in exchanges between ocean and ice shelves. *Oceanography*, **29 (4)**, 118–129.

Huang, R. X., 1993: Real freshwater flux as a natural boundary condition for the salinity balance and thermohaline circulation forced by evaporation and precipitation. *Journal of Physical Oceanography*, **23 (11)**, 2428–2446.

Jackson, R., and Coauthors, 2020: Meltwater intrusions reveal mechanisms for rapid submarine melt at a tidewater glacier. *Geophysical Research Letters*, **47 (2)**, e2019GL085 335.

Jacobs, S. S., A. Jenkins, C. F. Giulivi, and P. Dutrieux, 2011: Stronger ocean circulation and increased melting under pine island glacier ice shelf. *Nature Geoscience*, **4 (8)**, 519–523.

Jenkins, A., 1991: A one-dimensional model of ice shelf-ocean interaction. *Journal of Geophysical Research: Oceans*, **96 (C11)**, 20 671–20 677.

Jenkins, A., 2011: Convection-driven melting near the grounding lines of ice shelves and tidewater glaciers. *Journal of Physical Oceanography*, **41 (12)**, 2279–2294.

Jenkins, A., P. Dutrieux, S. S. Jacobs, S. D. McPhail, J. R. Perrett, A. T. Webb, and D. White, 2010: Observations beneath pine island glacier in west antarctica and implications for its retreat. *Nature Geoscience*, **3 (7)**, 468.

Jiang, H., and J. A. Breier, 2014: Physical controls on mixing and transport within rising submarine hydrothermal plumes: A numerical simulation study. *Deep Sea Research Part I: Oceanographic Research Papers*, **92**, 41–55.

Jones, J. M., and Coauthors, 2016: Assessing recent trends in high-latitude southern hemisphere surface climate. *Nature Climate Change*, **6 (10)**, 917–926.

Kim, I., D. Hahm, T. S. Rhee, T. W. Kim, C.-S. Kim, and S. Lee, 2016: The distribution of glacial meltwater in the amundsen sea, antarctica, revealed by dissolved helium and neon. *Journal of Geophysical Research: Oceans*, **121 (3)**, 1654–1666.

Kostov, Y., D. Ferreira, K. C. Armour, and J. Marshall, 2018: Contributions of greenhouse gas forcing and the southern annular mode to historical southern ocean surface temperature trends. *Geophysical Research Letters*, **45 (2)**, 1086–1097.

Lavelle, J., 1995: The initial rise of a hydrothermal plume from a line segment source—results from a three-dimensional numerical model. *Geophysical research letters*, **22 (2)**, 159–162.

Lazeroms, W., A. Jenkins, H. Gudmundsson, and R. van de Wal, 2018: Modelling present-day basal melt rates for antarctic ice shelves using a parametrization of buoyant meltwater plumes. *The Cryosphere*, **12 (1)**, 49–70.

Loose, B., P. Schlosser, W. Smethie, and S. Jacobs, 2009: An optimized estimate of glacial melt from the ross ice shelf using noble gases, stable isotopes, and cfc transient tracers. *Journal of Geophysical Research: Oceans*, **114 (C8)**.

Losch, M., 2008: Modeling ice shelf cavities in az coordinate ocean general circulation model. *Journal of Geophysical Research: Oceans*, **113 (C8)**.

MacAyeal, D. R., 1985: Evolution of tidally triggered meltwater plumes below ice shelves. *Oceanology of the Antarctic continental shelf*, **43**, 133–143.

Marshall, J., A. Adcroft, C. Hill, L. Perelman, and C. Heisey, 1997: A finite-volume, incompressible navier stokes model for studies of the ocean on parallel computers. *Journal of Geophysical Research: Oceans*, **102 (C3)**, 5753–5766.

Mathiot, P., A. Jenkins, C. Harris, and G. Madec, 2017: Explicit and parametrised representation of under ice shelf seas in az* coordinate ocean model nemo 3.6. *Geoscientific Model Development*, **10 (7)**, 2849–2874.

Morton, B., G. I. Taylor, and J. S. Turner, 1956: Turbulent gravitational convection from maintained and instantaneous sources. *Proceedings of the Royal Society of London. Series A. Mathematical and Physical Sciences*, **234 (1196)**, 1–23.

Naveira Garabato, A. C., and Coauthors, 2017: Vigorous lateral export of the meltwater outflow from beneath an antarctic ice shelf. *Nature*, **542 (7640)**, 219.

Olbers, D., and H. Hellmer, 2010: A box model of circulation and melting in ice shelf caverns. *Ocean Dynamics*, **60 (1)**, 141–153.

Paolo, F. S., H. A. Fricker, and L. Padman, 2015: Volume loss from antarctic ice shelves is accelerating. *Science*, **348 (6232)**, 327–331.

Pauling, A. G., C. M. Bitz, I. J. Smith, and P. J. Langhorne, 2016: The response of the southern ocean and antarctic sea ice to freshwater from ice shelves in an earth system model. *Journal of Climate*, **29 (5)**, 1655–1672.

Pelle, T., M. Morlighem, and J. H. Bondzio, 2019: Brief communication: Picop, a new ocean melt parameterization under ice shelves combining pico and a plume model. *The Cryosphere*, **13 (3)**, 1043–1049.

Prince, P. J., and J. R. Dormand, 1981: High order embedded runge-kutta formulae. *Journal of Computational and Applied Mathematics*, **7 (1)**, 67–75.

Ramadhan, A., and Coauthors, 2020: Oceananigans.jl: Fast and friendly geophysical fluid dynamics on gpus. *Journal of Open Source Software*, **5 (53)**, 2018.

Reese, R., T. Albrecht, M. Mengel, X. Asay-Davis, and R. Winkelmann, 2018: Antarctic sub-shelf melt rates via pico.

Rignot, E., J. Mouginot, B. Scheuchl, M. van den Broeke, M. J. van Wessem, and M. Morlighem, 2019: Four decades of antarctic ice sheet mass balance from 1979–2017. *Proceedings of the National Academy of Sciences*, **116 (4)**, 1095–1103.

Roquet, F., G. Madec, L. Brodeau, and J. Nycander, 2015: Defining a simplified yet "realistic" equation of state for seawater. *Journal of Physical Oceanography*, **45 (10)**, 2564–2579.

Rozema, W., H. J. Bae, P. Moin, and R. Verstappen, 2015: Minimum-dissipation models for large-eddy simulation. *Physics of Fluids*, **27 (8)**, 085 107.

Rye, C. D., A. C. N. Garabato, P. R. Holland, M. P. Meredith, A. G. Nurser, C. W. Hughes, A. C. Coward, and D. J. Webb, 2014: Rapid sea-level rise along the antarctic margins in response to increased glacial discharge. *Nature Geoscience*, **7 (10)**, 732.

Rye, C. D., J. Marshall, M. Kelley, G. Russell, L. S. Nazarenko, Y. Kostov, G. A. Schmidt, and J. Hansen, 2020: Antarctic glacial melt as a driver of recent southern ocean climate trends. *Geophysical Research Letters*.

Sciascia, R., F. Straneo, C. Cenedese, and P. Heimbach, 2013: Seasonal variability of submarine melt rate and circulation in an east greenland fjord. *Journal of Geophysical Research: Oceans*, **118 (5)**, 2492–2506.

Slater, D., P. Nienow, T. Cowton, D. Goldberg, and A. Sole, 2015: Effect of near-terminus subglacial hydrology on tidewater glacier submarine melt rates. *Geophysical Research Letters*, **42 (8)**, 2861–2868.

Speer, K. G., and J. Marshall, 1995: The growth of convective plumes at seafloor hot springs. *Journal of marine research*, **53 (6)**, 1025–1057.

Swart, N., and J. Fyfe, 2013: The influence of recent antarctic ice sheet retreat on simulated sea ice area trends. *Geophysical Research Letters*, **40 (16)**, 4328–4332.

Taylor, K. E., R. J. Stouffer, and G. A. Meehl, 2012: An overview of cmip5 and the experiment design. *Bulletin of the American Meteorological Society*, **93 (4)**, 485–498.

Thurnherr, A. M., S. Jacobs, P. Dutrieux, and C. Giulivi, 2014: Export and circulation of ice cavity water in pine island bay, west antarctica. *Journal of Geophysical Research: Oceans*, **119 (3)**, 1754–1764.

Turner, J., 1986: Turbulent entrainment: the development of the entrainment assumption, and its application to geophysical flows. *Journal of Fluid Mechanics*, **173**, 431–471.

Turner, J., T. J. Bracegirdle, T. Phillips, G. J. Marshall, and J. S. Hosking, 2013: An initial assessment of antarctic sea ice extent in the cmip5 models. *Journal of Climate*, **26 (5)**, 1473–1484.

Vallis, G. K., 2017: *Atmospheric and oceanic fluid dynamics*. Cambridge University Press.

Verstappen, R., 2018: How much eddy dissipation is needed to counterbalance the nonlinear production of small, unresolved scales in a large-eddy simulation of turbulence? *Computers & Fluids*, **176**, 276–284.

Vreugdenhil, C. A., and J. R. Taylor, 2018: Large-eddy simulations of stratified plane couette flow using the anisotropic minimum-dissipation model. *Physics of Fluids*, **30 (8)**, 085 104.

Xu, Y., E. Rignot, I. Fenty, D. Menemenlis, and M. M. Flexas, 2013: Subaqueous melting of store glacier, west greenland from three-dimensional, high-resolution numerical modeling and ocean observations. *Geophysical Research Letters*, **40 (17)**, 4648–4653.

Xu, Y., E. Rignot, D. Menemenlis, and M. Koppes, 2012: Numerical experiments on subaqueous melting of greenland tidewater glaciers in response to ocean warming and enhanced subglacial discharge. *Annals of Glaciology*, **53 (60)**, 229–234.

# LIST OF FIGURES

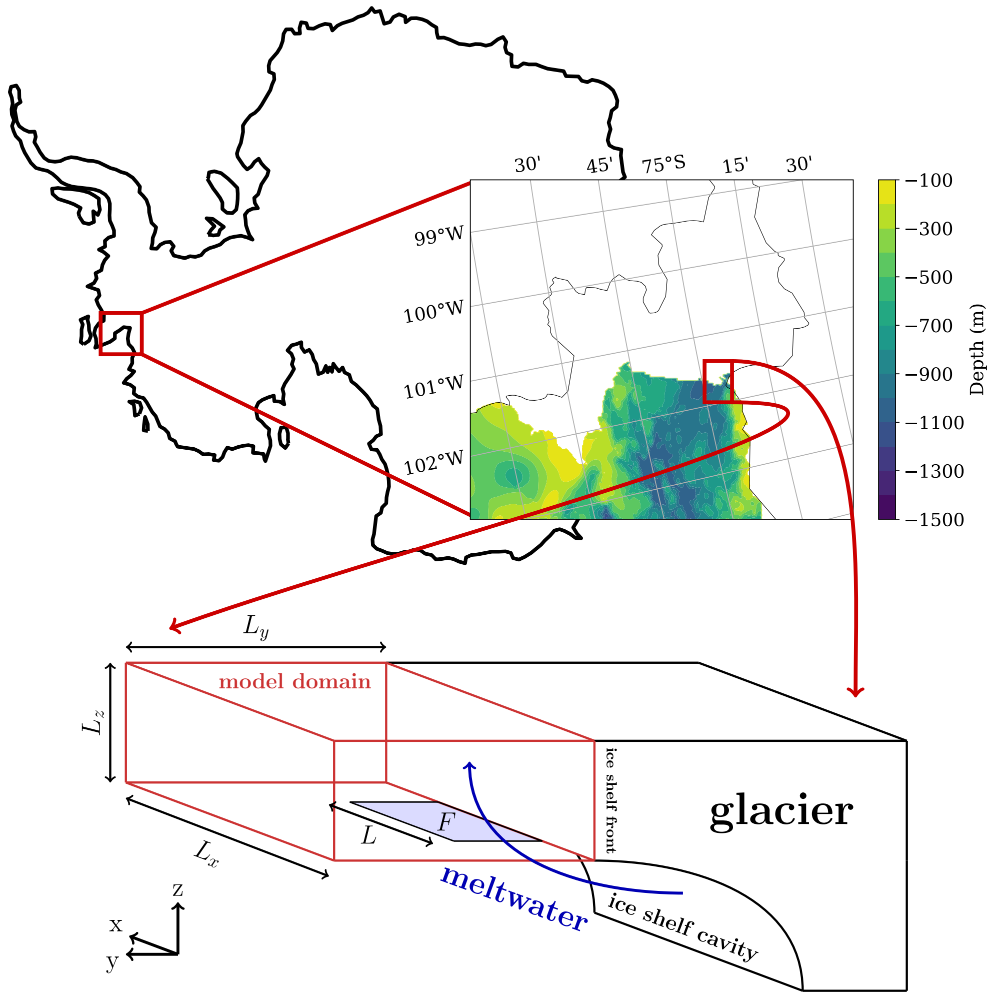


643 FIG. 1. A schematic describing the object of study. Much of the total mass loss from the Antarctic ice sheet stems from a small number of rapidly-melting ice shelves; here we highlight the Pine Island ice shelf as an example. The meltwater escaping from underneath the ice shelf is concentrated in a narrow km-scale outflow at its western edge; this is likely a generic feature of many Antarctic ice shelves. We idealize this meltwater outflow as a constant buoyancy source $F$, with width $L$, applied to the bottom of our model domain.

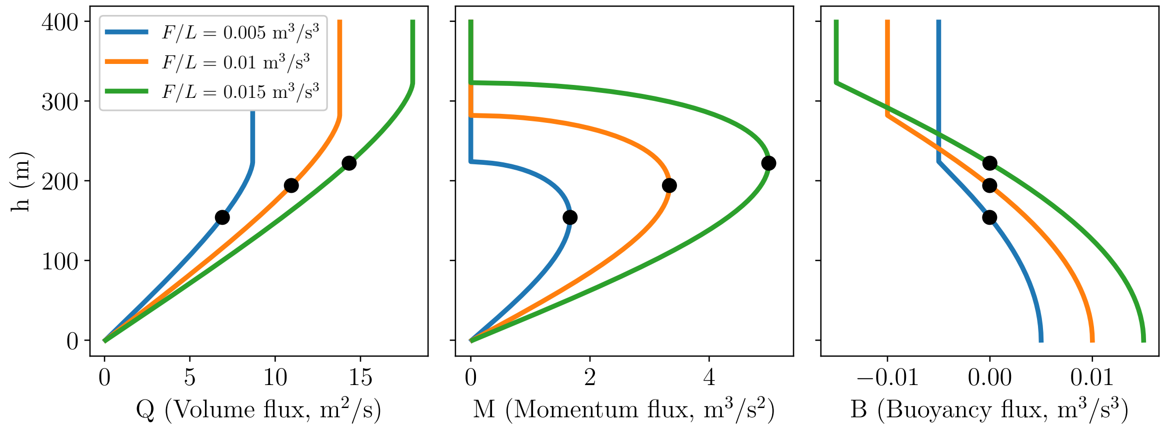


FIG. 2. Example solutions of the one-dimensional line plume model for different buoyancy forcings $F/L$. $h = 0$ represents the base of the ice shelf front. In each case, the black dot highlights the meltwater's settling depth; this is the level of neutral buoyancy, i.e. where $B(z) = 0$

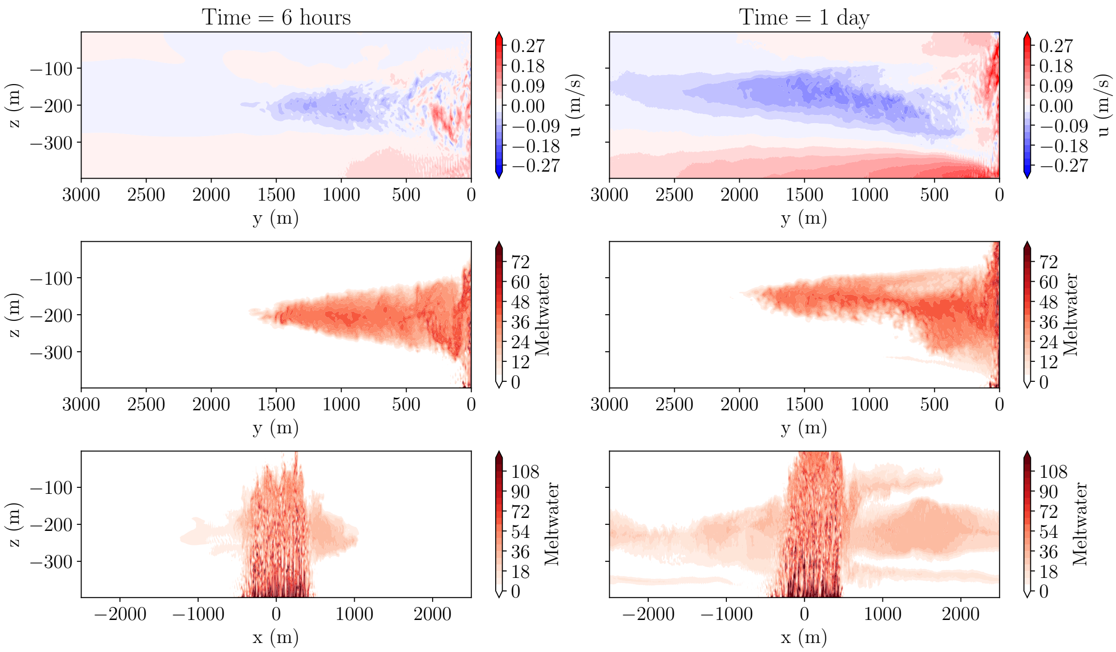


FIG. 3. Evolution of a simulated meltwater plume, after 6 hours and after one day. The meltwater concentrations are in arbitrary units. The upper two rows depict a $yz$-plane with $x = 0$ (i.e. perpendicular to the ice shelf front). The bottom row depicts an $xz$-plane with $y = 0$ (i.e. along the ice shelf front). A strong zonal flow develops: this is consistent with observations of the outflow from beneath the Pine Island ice shelf. The zonal flow is responsible for the transport of meltwater in the $x$-direction that can be observed in the bottom right plot: the meltwater outflow is deflected to the west by the Coriolis force, and eventually re-enters the domain at the eastern boundary.

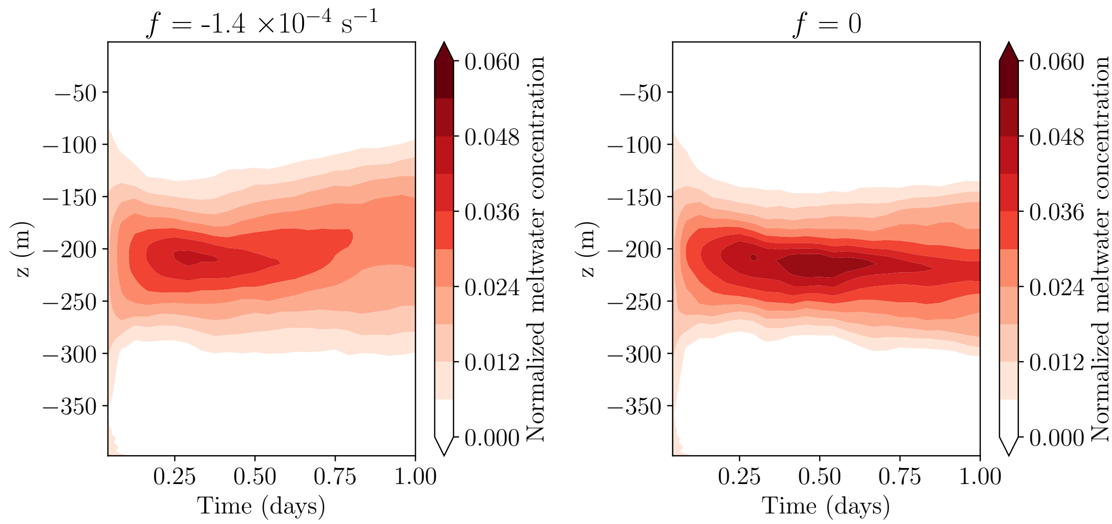


FIG. 4. The evolution of the horizontally averaged vertical meltwater distribution over 1 day of simulation, for a realistic value of the Coriolis parameter $f$ and for a case where $f = 0$. Here, $F/L = 10^{-2}$ m$^3$/s$^3$. We see that the primary role of rotational effects is to broaden the distribution of meltwater over a wider range of depths, suggesting that they play an important mixing role. However, they do not appear to have a substantial effect on the mean settling depth.

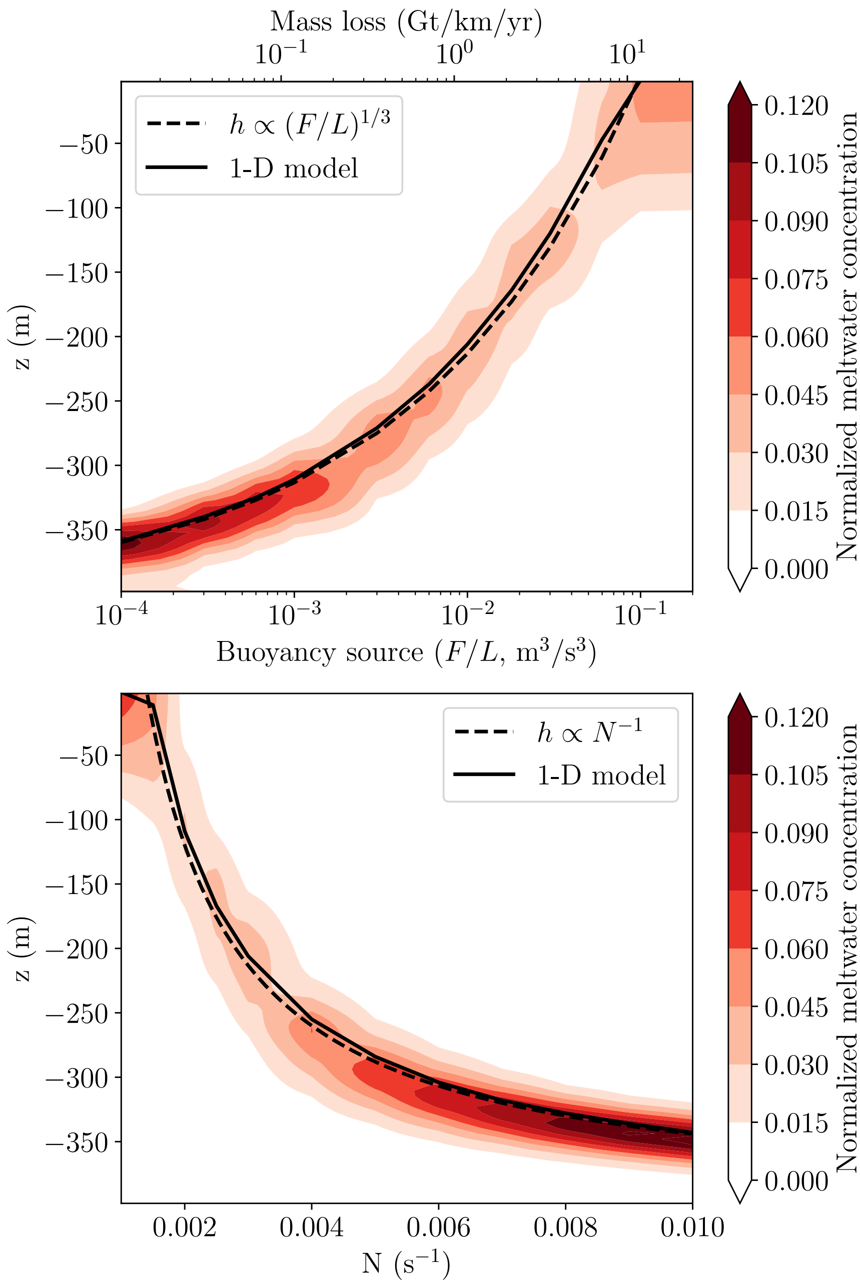


FIG. 5. The horizontally averaged vertical meltwater distribution after 6 hours of simulation, for varying buoyancy source $F/L$ and buoyancy frequency $N$. For the case of varying $F/L$, we have also estimated an equivalent mass loss flux (see text). On top of the distributions we plot the settling depths predicted by the simple scaling relationship (dashed) and the one-dimensional line plume model (solid): both show excellent agreement with the high-resolution simulations.

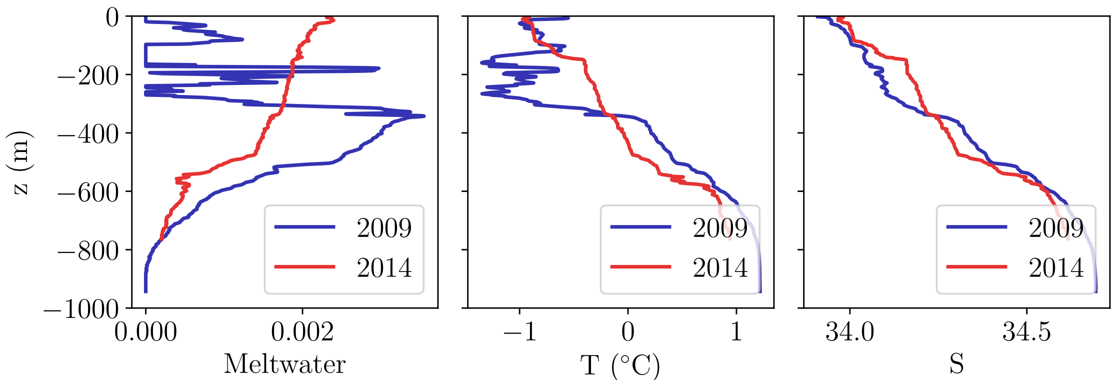


FIG. 6. Observed 2009 and 2014 temperature and salinity profiles next to the meltwater outflow from Pine Island Glacier, as well as estimated meltwater fractions. In 2009, meltwater was primarily centered at a 400m depth, while in 2014 it was able to rise to the surface.

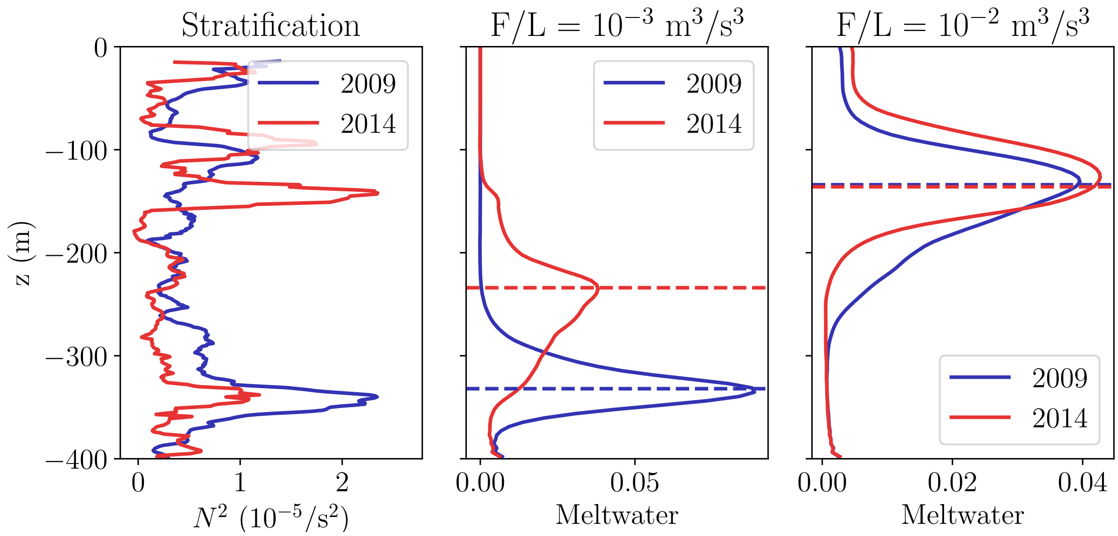


FIG. 7. Simulated vertical meltwater distributions for $F/L = 10^{-3}$ m$^3$/s$^3$ and $F/L = 10^{-2}$ m$^3$/s$^3$, with initial conditions set by observed temperature and salinity profiles for 2009 and 2014. Horizontal dashed lines indicate the settling depths predicted by the one-dimensional line plume model for the same conditions; notably, the line plume model accurately predicts the peak of the simulated meltwater distribution in all cases. We also plot depth profiles of stratification strength in terms of $N^2$ (see text). For $F/L = 10^{-2}$ m$^3$/s$^3$ we see that there is little difference in the vertical meltwater distribution between 2009 and 2014 conditions. However, the simulations with $F/L = 10^{-3}$ m$^3$/s$^3$ show a marked difference: the qualitative trend is consistent with observations (Figure 6). Here, we propose that the rising meltwater was "trapped" by the notable local stratification maximum at around 350m depth in the 2009 conditions.

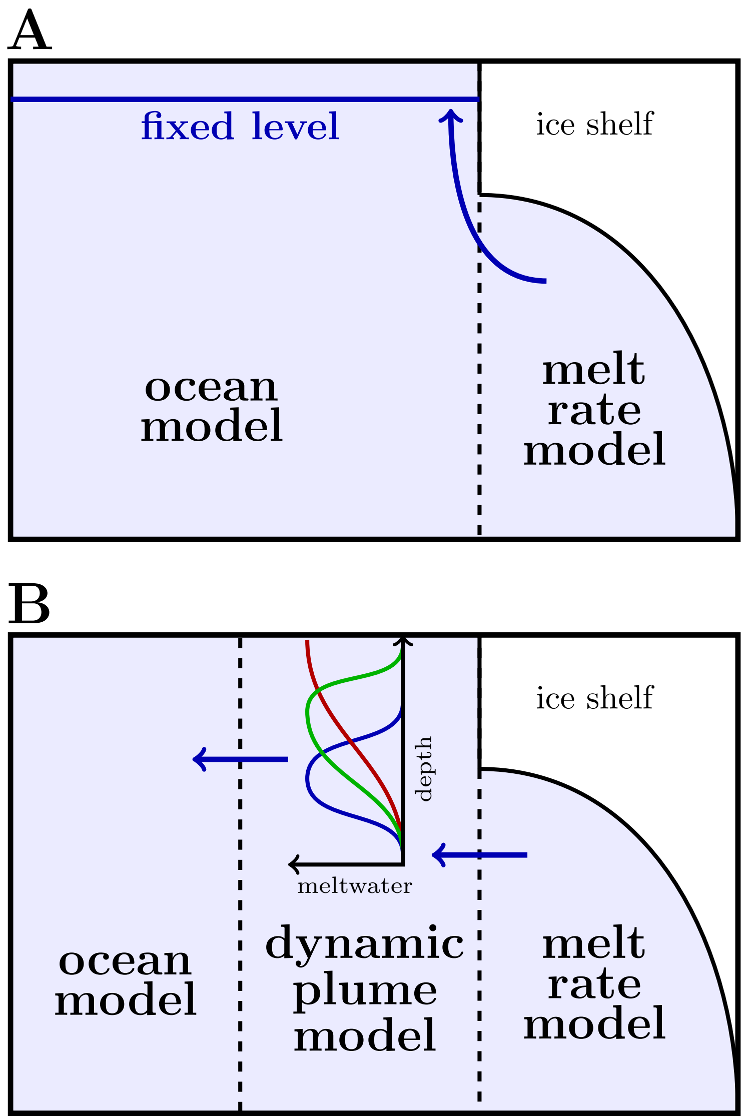


680 Fig. 8. Schematic describing two different paradigms for meltwater fluxes in simulations of global climate. In paradigm A, the fluxes from a melt rate model are inserted into the ocean model at some fixed vertical level; this approach has dominated the literature. In paradigm B, the melt rate model is coupled to a dynamic plume model that describes the small-scale dynamics of buoyant meltwater plumes and accurately calculates the vertical distribution of meltwater for insertion into the ocean model. Given the potential climatic importance of glacial meltwater, the strong dependence of settling depth on the buoyancy forcing, and the vast heterogeneity in the observed mass loss rates from different ice shelves, this approach would likely represent a significant improvement over the “one-size-fits-all" approach of paradigm A.

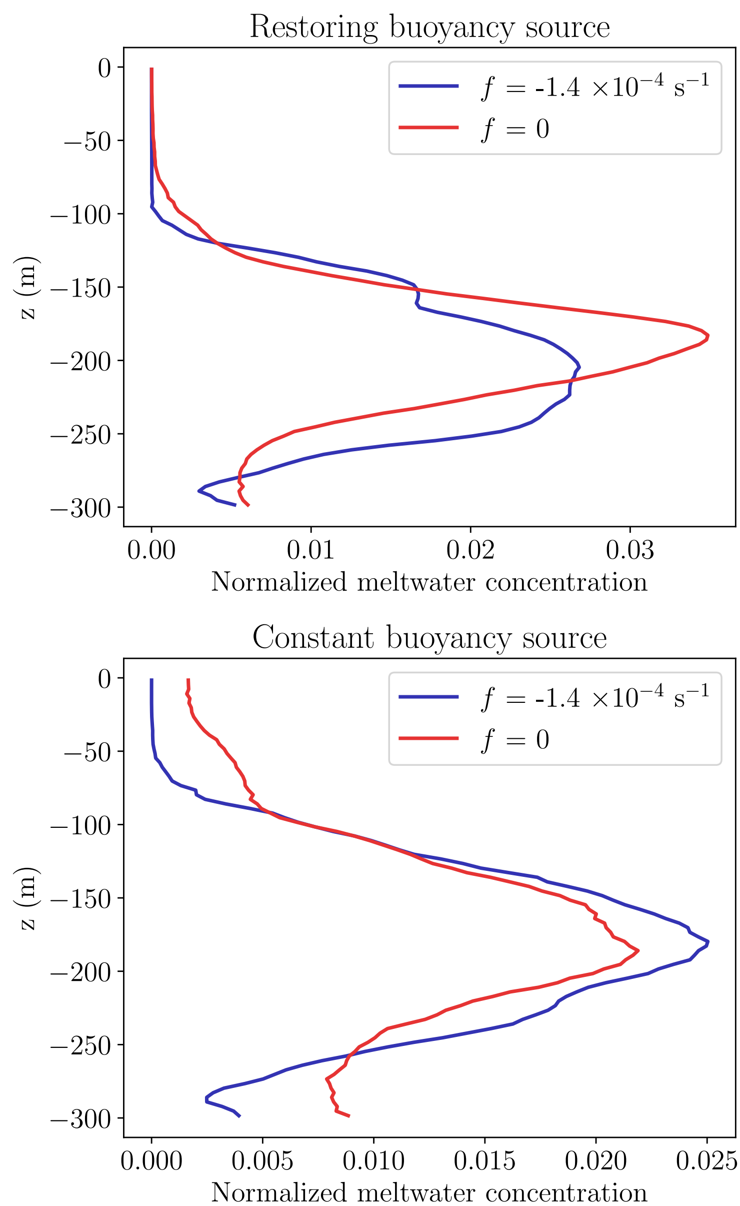


FIG. 9. Vertical meltwater distributions, for rotating and non-rotating cases, in a two-dimensional domain. On the top, we have introduced meltwater via a restoring buoyancy source (following Naveira Garabato et al. (2017), see text), while on the bottom we have used a constant buoyancy source (as in the simulations described in the main text). When a constant buoyancy source is employed, the peak of the vertical distribution is not noticeably influenced by the effects of rotation. However, when a restoring buoyancy source is employed, rotation deepens the peak by ~ 50 m, consistent with the simulations of Naveira Garabato et al. (2017). Since the magnitude of the buoyancy source is a primary control on the meltwater's settling depth, the importance of any other parameters can only be accurately investigated by holding the buoyancy source constant; therefore, these results show that the use of restoring non-constant buoyancy sources may exaggerate the effect of rotation on the settling depth.